



# Ultra strong FCC structured Ni<sub>8</sub>Cr<sub>4</sub>Co<sub>4</sub>Fe<sub>6</sub>W<sub>2</sub> high entropy alloys with high strength and ductility by laser powder bed fusion

Zhen Gu<sup>a</sup>, Jiayu He<sup>a</sup>, Yuanbin Qin<sup>a</sup>, Peng Zhang<sup>a</sup>, Pengcheng Zhang<sup>a</sup>, Danli Zhang<sup>a</sup>, Hongjing Wu<sup>a</sup>, L.L. Xiao<sup>b,\*</sup>, Shengqi Xi<sup>a</sup>

<sup>a</sup> State Key Laboratory for Mechanical Behavior of Materials, School of Material Science and Engineering, Xi'an Jiaotong University, Xi'an 710049, PR China

<sup>b</sup> Institute of Materials, Henan Academy of Sciences, Zhengzhou 450046, PR China



## ARTICLE INFO

**Keywords:**  
Powder bed fusion  
Ni<sub>8</sub>Cr<sub>4</sub>Co<sub>4</sub>Fe<sub>6</sub>W<sub>2</sub>  
Solute homogenization  
Strain rate sensitivity  
Mechanical properties

## ABSTRACT

The high entropy alloys (HEAs) are widely used in high temperature service environment (such as aviation engine blades) with bright application potential in additive manufacturing. Laser powder bed fusion (LPBF) is technology currently offers the best reproducibility and dimensional accuracy for part production. The unique atomic lattice structure of HEA makes its plastic deformation mechanism different from that of traditional dilution alloy, resulting in the strengthening effect of face-centered cubic high-entropy alloy different from that of traditional metal alloy materials. In this paper, Ni<sub>8</sub>Cr<sub>4</sub>Co<sub>4</sub>Fe<sub>6</sub>W<sub>2</sub> was designed by means of composition control. Its spherical powders with uniform composition were successfully prepared by high temperature remelting spheroidization (PHTR) method, compared with gas atomization (GA) method. The strain rate sensitivity  $m$  values of GA-Selective Laser Melting and PHTR-Selective Laser Melting samples were 0.030 and 0.027, respectively. The hardness of Ni<sub>8</sub>Cr<sub>4</sub>Co<sub>4</sub>Fe<sub>6</sub>W<sub>2</sub> high-entropy alloy showed a trend of continuous increase with the decrease of grain size, while the elastic modulus didn't change much (PHTR-SLM is 193 Gpa and GA-SLM is 189 Gpa). The simulated value of the contact stress decreased by 23 % compared with the theoretical value. The contact radius increased with the increase of plastic deformation in addition to the reduction of contact pressure. The printing sample value of the elongation, yield strength (YS) and Ultimate Tensile Strength (UTS) on PHTR-SLM has increased by 39.6 %, 33.7 % and 25.9 %, respectively in additive manufacturing, compared to GA-SLM. The ability to produce refractory HEAs through PHTR method will make it possible to manufacture complex geometry shapes at a reasonable cost.

## 1. Introduction

The high entropy alloy (HEAs) has a simple solid solution structure, which can avoid the formation of a large number of intermetallic compounds [1–5]. The high entropy alloys (HEAs) are widely used in high temperature service environment (such as aviation engine blades) with bright application potential in additive manufacturing. [6,7]. High entropy alloys containing refractory elements (Cr-W, W-Cu, etc. [5–8]) show the excellent characteristics of high strength, high temperature stability and thermal conductivity etc. Laser powder bed fusion (LPBF) is technology currently offers the best reproducibility and dimensional accuracy for part production. Therefore, it has been well studied in both industry and academia. [9–12]. The plastic deformation behavior of alloy materials containing refractory elements and its dependence on grain size has been widely concerned [13]. Understanding and

predicting plastic deformation mechanisms, especially those related to grain boundaries, is critical to the design of metal materials [14].

Different from conventional alloys, the difference of atomic arrangement and related stress field between intergranular regions and grain boundaries of high entropy alloys is relatively small. The difference between grain boundary and intrachrystalline region in high entropy alloys is not significant. Even if the grain size has been reduced to a very small nanometer scale, the difference between the microstructure and internal stress in the grain and the grain boundary is not as significant as that in diluted alloys and pure metals. Therefore, the unique atomic lattice structure of high-entropy alloy makes its plastic deformation mechanism different from that of traditional dilution alloy [15], resulting in the strengthening effect of face-centered cubic HEAs different from that of traditional metal alloy materials. A lot of studies have been conducted on the influence of configurational entropy [16],

\* Corresponding authors.

E-mail addresses: [xiaolili375@163.com](mailto:xiaolili375@163.com) (L.L. Xiao), [xixishengqi@126.com](mailto:xixishengqi@126.com) (S. Xi).

phase separation [17], solid solution [18] and other factors, insufficient attention has been paid to the changes in grain boundary and intra-granular differences caused by the randomness of HEAs substructure [19]. Due to the different atomic radii of the component elements, the level of isotropic distortion field generated in HEA is particularly high, pushing nearby atoms away from their ideal position [20].

At present, the gas atomization method (GA) is the main processes for preparing alloy powder required for additive manufacturing. With the cooling effect of inert gas (argon or helium), the spherical metal powder is formed by rapid solidification [21–24]. The alloy powder of refractory element system requires high melting temperature. But the temperature of induction melting furnace is difficult to exceed the melting point of refractory element (1400–3300 °C). Thus, there are a few unmelted refractory powder particles in the prepared metal ingot. After an ultra-short-term rapid melting and cooling process, the elements in the final spherical powder will have segregation. As a result, such process often produces refractory alloy powder with uneven composition, affecting the quality and performance of specimens. In addition, the alloy powders obtained by this process inevitably have defects, such as oxide inclusions and satellite particles. Therefore, the study and preparation of high quality refractory alloy powders with uniform composition has been one of the key development directions in additive manufacturing field.

In this paper, spherical high entropy alloy powders were prepared by a new technology, aiming at composition uniformity. However, powders with uniform composition cannot be used to evaluate the performance of the final products. Based on this, the authors have carried out additive manufacturing technology to study the mechanical properties of the forming parts and the raw materials are prepared by high temperature remelting spheroidization (PHTR) method. This technology is of great significance for the development of high performance HEA alloy powder, optimization of processing technology, perfection and composition evolution research. It seems that the high entropy alloy powder obtained by PHTR method can homogenize the internal composition. Thus, The high entropy alloy spherical powders ( $\text{Ni}_8\text{Cr}_4\text{Co}_4\text{Fe}_6\text{W}_2$ ) prepared by these two methods were used to print the forming parts by additive manufacturing. Table 1 shows the parameters of each group of high entropy alloy. In this study, the possibility of synthesizing refractory HEA  $\text{Ni}_8\text{Cr}_4\text{Co}_4\text{Fe}_6\text{W}_2$  from mixed element alloy powder by PHTR process was investigated. The evaluation includes the preparation of 3D forming parts with the same chemical composition by conventional GA processes as a reference. The ability to produce refractory HEAs through PHTR method will make it possible to manufacture complex geometry shapes at a reasonable cost.

## 2. Materials and methods

### 2.1. Material selection

For the newly designed Ni-Fe-Cr-Co-W high entropy alloy system, we used the mechanical alloy powders obtained by high-energy rod milling machine. The particle size of the original elemental powder required in this paper is 60–80  $\mu\text{m}$  with purity of 99.95 %. Q235 was used as the base material (BM) with a size of 300 mm × 100 mm × 10 mm. The composition of the substrate is shown in Table 2.

**Table 1**  
Parameter characteristics of components in high entropy alloys.

Element	Atomic radius/ $\text{\AA}$	Crystal structure	Electro-negativity	Melting point/°C	Valence Electron Concentration	Density/(g/cm <sup>3</sup> )
Ni	1.2459	FCC	1.91	1453	10	8.90
Cr	1.2491	BCC	1.70	1857	6	7.19
W	1.3670	BCC	2.36	3410	6	19.35
Fe	1.2412	BCC	1.83	1538	8	7.86
Co	1.2518	HCP	1.88	1495	9	8.90

**Table 2**  
Composition of Q235 stainless steel.

Element	C	Mn	Si	S	P
Mass percentage/%	0.14–0.22	0.30–0.65	≤ 0.3	≤ 0.05	≤ 0.045

### 2.2. Preparation of alloy powder

The powder is first alloyed by mechanical alloying technology. The combination of mechanical grinding (plastic deformation) and temperature raising (atomic diffusion) results in the homogenization of alloy powder composition. Before the rod mill is in operation, the milling tank is filled with protective gas (Ar). On the one hand, it can protect the powder from being oxidized during. On the other hand, it makes the atmospheric pressure inside and outside the tank in a balanced state, preventing the explosion caused by the internal temperature sudden rise in the process of high-energy operation. Alcohol is generally used for wet extraction, effectively oxidizing the powder during the powder extraction process.

After mechanical alloying treatment, the mechanically alloyed powders in the feeder are continuously fed into the high temperature falling channel by a spiral feeder. The powder is evenly dispersed in the shielding gas (Ar, 120 ml·min<sup>-1</sup>). As it passes through the plasma nozzle, the falling metal particles are rapidly heated and melt into droplets. Under the action of surface tension, metals spontaneously concentrate into spheres. At last, we get the so called Plasma high-temperature melting (PHTR) powder. Table 3 is the chemical composition of the GA-powder; PHTR-powder, respectively. The powders are examined by X-ray Fluorescence Spectrometer.

### 2.3. Feeding rate of PHTR

When powder particles start to fall down from the plasma nozzle, It is important for the screw speed to determine the total amount of powders by PHTR method. In this experiment, Malvern laser particle size analyzer was used to measure the particle size distribution of alloy powder at different rotational speeds (Fig. 1). The fluidity of treated alloy powder is 2.436 g/min, 2.176 g/min, 1.735 g /min and 1.329 g /min, respectively. D10, D50, D90 parameters for each particle size distribution measurement are shown in Table 4.

### 2.4. HEA sample fabrication

The sample was cut into the required shape for tensile test, micro-structure observation, wear test, etc (see Fig. 2).

The average particle size of these two alloyed spherical powder

**Table 3**  
Chemical composition of the  $\text{Ni}_8\text{Cr}_4\text{Co}_4\text{Fe}_6\text{W}_2$  HEA powders and printing samples (wt%).

Element	Ni	W	Cr	Fe	Co
Theoretical component	29.06	22.75	12.87	20.74	14.59
GA Powder	23.43	26.91	13.27	32.11	4.16
PHTR Power	25.17	23.88	12.93	34.28	3.65

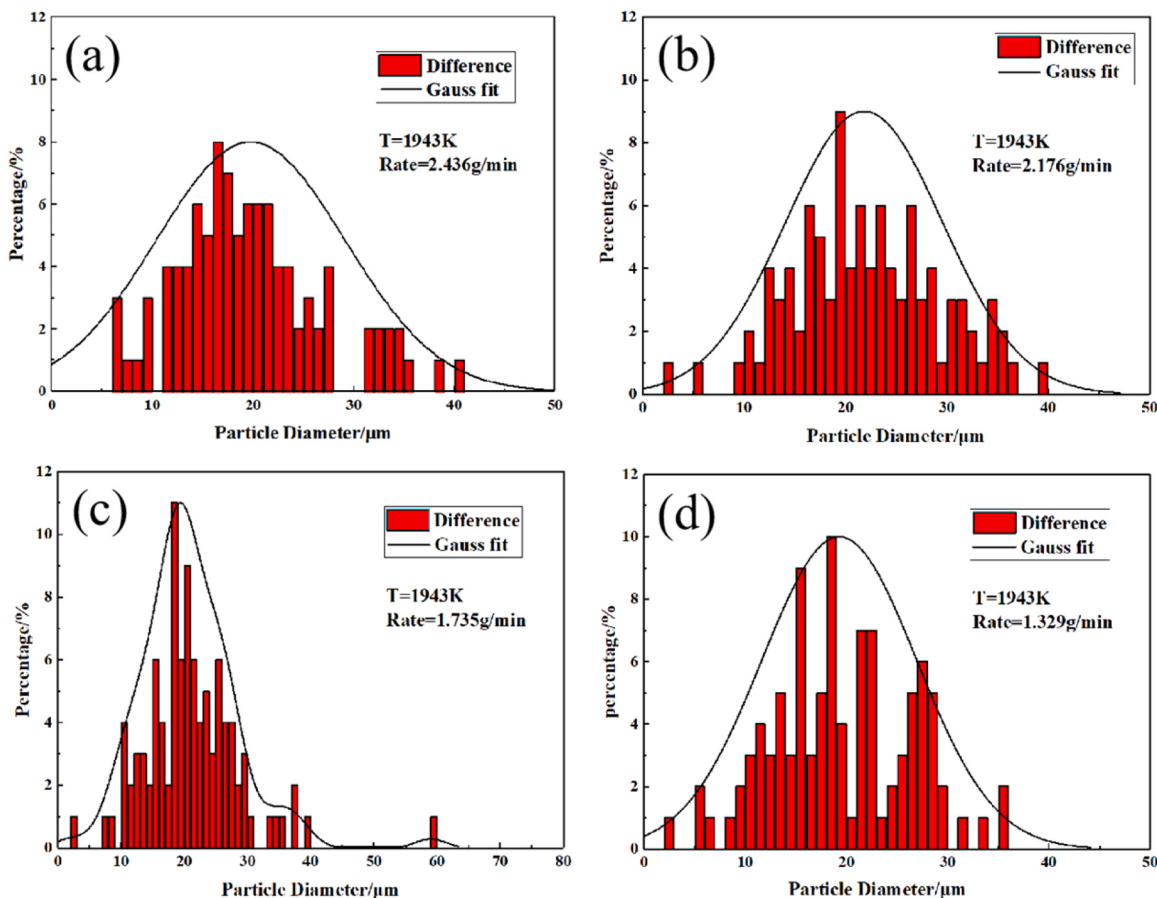


**Fig. 1.** Particle size distribution of HEA-PHTR powder (a) feed at 2.436 g/min, (b) feed at 2.176 g/min, (c) feed at 1.735 g/min, (d) feed at 1.329 g/min.

**Table 4**

The HEA-PHTR particle size distribution measurement at different feed rate.

Powder feed rate	2.436 g/min	2.176 g/min	1.735 g/min	1.329 g/min
D10	8.42 μm	8.93 μm	9.77 μm	9.91 μm
D50	19.03 μm	20.43 μm	21.66 μm	19.69 μm
D90	39.65 μm	37.58 μm	58.17 μm	35.42 μm

(PHTR powder and GA powder) is 15–38 μm. Ar (shielding gas, 99.995 %) remains a flow rate of 8 L/min. All designed alloyed are fabricated by the selective laser melting equipment (SLM 260, Xi'an Jiaotong University, China) and its manufacturing room is 100×100×100 mm<sup>3</sup>. As for the laser condition: laser wavelength is 1.07 μm, the thickness of each layer is 0.05 mm, the spot diameter decides the beam size and spot diameter is 0.1 mm. Maximum pulse

energy: 1.2 MJ. Beam quality (M2 < 1.1), spot accuracy up to 0.2 deg. The energy distribution of the spot is uniform. Operating environment: 100 ~ 240 V, 50 Hz, 180 W. GA-powder and PHTR-powder were manufactured under the same conditions with the same printing parameters. The best experimental parameters determined by orthogonal experiment are as follows: laser power is 420 W, scanning speed is 25,000 mm/s, the powder layer thickness is 0.05 mm, and scanning space is 120 μm. laser wavelength is 1.07 μm. The scanning angle θ is preset at 90°(The scan direction is perpendicular to the X-axis). The LPBF technology uses the following steps to fabricate components:(1) A layer of metal powder of a specified thickness is laid on the building board inside the machine; (2) Selectively melt the desired region within the powder layer with a laser beam; (3) Move the building board down and spread a new layer of powder on the building board. This process is repeated layer by layer until the part is manufactured. The blocks are modified by using a wire cutting machine to obtain the required size.

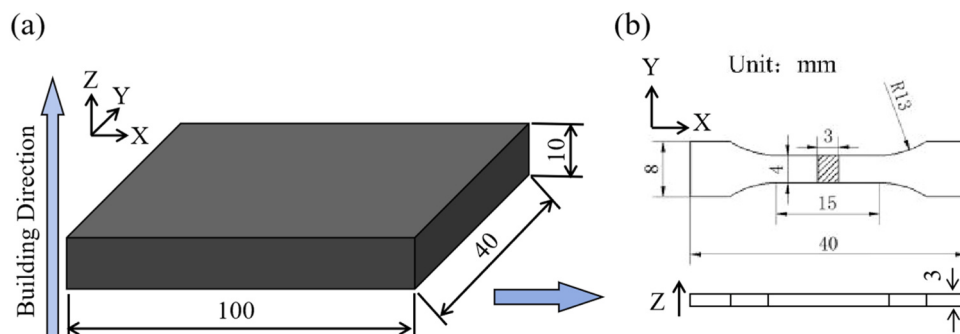


**Fig. 2.** Testing samples.

The samples were first cut into  $10 \times 10 \times 6$  mm testing blocks. We use different type of sand papers and polishing machines (IntroSmart RV200, China) to make the printing metal surface smooth and scratch free.

## 2.5. Material characterization tests

Tensile samples were prepared according to the Tensile Test Standard for Metallic Materials (GB/T 228–2002). The testing machine has been used with an elongator at a loading rate of  $0.5 \text{ mm} \cdot \text{min}^{-1}$ . The phase was tested by X-ray diffractometer (XRD, PANalytical X'Pert S-MPD, Netherlands) with Cu-K $\alpha$  ray wavelength is  $\lambda = 0.154072 \text{ nm}$ . The microstructure was characterized by Scanning Electron Microscope (SEM) (JSM-8000 F, Japan), EDS (JSM-8000 F, Japan) and Transmission Electron Microscope (TEM) (JEOLJEM-1800Plus, Netherlands). The SU3500 Electron back scatter diffractometer (EBSD) was used to test the middle parts of the tensile sample. The Nanoindenter XP® system, manufactured by MTS, was used to characterize the mechanical properties of bulk high entropy alloys. Berkovich diamond indenter was used as the indenter for the nanoindentation test. The radius of the indenter tip was determined to be  $\sim 50 \text{ nm}$  by the fused quartz standard sample. The Continuous Stiffness Measurement (CSM) method, which can continuously record the elastic modulus and hardness in the direction of pressing depth, was used to perform nanoindentation test on the single phase Ni<sub>8</sub>Cr<sub>4</sub>Co<sub>4</sub>Fe<sub>6</sub>W<sub>2</sub> high entropy alloy printing samples, and the relevant mechanical parameters such as hardness and elastic modulus were obtained. The press depth control mode is selected, and the maximum press depth of the block sample is set to 1500 nm to eliminate the surface size effect. The two-body wear test is carried out on the pin-disk wear test machine (ml-100, Shanghai). The specimen is a flat cylinder with  $\phi 6 \text{ mm} \times 20 \text{ mm}$ . Al<sub>2</sub>O<sub>3</sub> abrasive coarse sandpaper (180#, 2400 HV) is fixed to the disc. In the experiment, the slip rate of the small cylindrical specimen is  $8 \text{ mm} \cdot \text{r}^{-1}$ , the rotation rate of the disk is  $72 \text{ r} \cdot \text{min}^{-1}$ , and the total distance of the spiral orbit in a spiral process is 7.6 m. SEM and color 3D laser scanning microscope (model VK-9710) are used to evaluate the wear resistance of different alloy specimens on the worn sample surface. The worn cylindrical specimen is treated with nickel plating to a thickness of approximately 50  $\mu\text{m}$ . Then it is cut in the vertical direction relative to the worn surface, and the microstructure characteristics of the vertical section are observed by SEM.

## 3. Results and discussion on HEA powders

### 3.1. The influence of powder morphology

In Fig. 3, the lamellar mechanical alloy Ni<sub>8</sub>Cr<sub>4</sub>Co<sub>4</sub>Fe<sub>6</sub>W<sub>2</sub> powders were subjected to plasma melt-blown gravity fall treatment at different temperatures, and its particle size and surface morphology could be observed by SEM. The results show that the spheroidization pattern is proportional to temperature in a certain range.

Spheroidization rate is regarded as one of the most important indexes to assess spheroidization quality. The spheroidizing effect is significantly improved with the increase of temperature. A large number of alloyed particles remain non-molten at 1773 K (The spheroidization rate is 29.8 %). When the temperature keeps among 1853 K, most of the particles melt into spherical shapes, while a small part of the particles do not melt into spheres (melting is not completed) with the form of short rods or irregular droplets. Within this temperature range, the particles have melted or are largely melted. Since these powders witness a rapid cooling rate after falling to the collecting device, there is not enough time for them to concentrate into sphere shapes. All the particles appear spherical and have bright surfaces at 1943 K, seen in Fig. 3c (The spheroidization rate exceeded 97.56 %). When the temperature reaches up to 1973 K, the spheroidization rate (98.86 %) is close to 100 %. Considered the cooling rate is also very high at the same time, it is suggested that powders don't have enough time to concentrate into a sphere. Therefore, the spheroidization rate can be guaranteed by properly increasing the temperature. In contrast, the powder obtained by GA method (Fig. 3d) is less spheroidized. The sphericity of the powder is lower than that obtained by PHTR method, and some powder bonding occurs. The distribution of temperature in the vertical direction of the pipe center line can be obtained by measurement and fitting.

Fig. 3e shows the relationship between the position of powder particles at different times and the atmosphere temperature. The settling time is 0.84 s for 12  $\mu\text{m}$  particles, and that of 2  $\mu\text{m}$  particles is 3.72 s. There are two main forces acting on the falling powder. The force of gravity going straight down and the drag going straight up. However, the resistance is affected by the state of particle motion and the thermal and physical parameters of the gas body. First, the particle falls freely under gravity ( $v = 1/2 at^2$ ). The gas viscosity increases rapidly in the high temperature region, and the particle velocity fluctuates greatly. The resistance increases gradually. This will cause the acceleration  $a$  to decrease and the particle velocity to decrease. Finally, gravity and drag reach a dynamic equilibrium, while the particle moves at a certain maximum velocity.

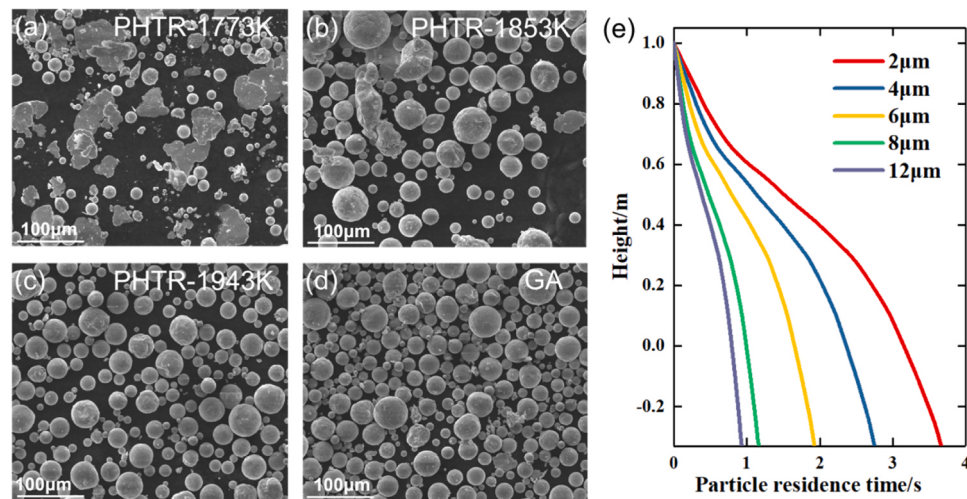


Fig. 3. Morphology (SEM) of the HEA powders treated under different temperatures.

### 3.2. Morphology and composition analysis of alloyed powders

**Fig. 4** shows the spherical cross-section morphology and energy spectrum of spherical particles obtained by plasma high-temperature remelting (PHTR) and gas atomization (GA), respectively. The surface distribution of spherical particles is not a good indication of the internal distribution of elements. Therefore, the authors used FIB to extract spherical particles and cut their cross sections for further characterization. It can be found that the distribution of elements in the alloyed powder does not appear segregation, showing homogenization by PHTR. The atoms near the grain boundary will become active and exchange with other atoms. As the atoms continue, the protons will leave their original positions and form supersaturated solid solutions. The researchers found local stress concentration between the powder particles will occur or defects happen with the continuous milling [25], leading to the reduction of the free energy of atomic diffusion. Atoms can more easily diffuse, accelerating the alloying and making the element distribution more uniform.

In contrast, only Fe and Ni elements are evenly distributed in the powder obtained by GA (**Fig. 4b**). However, component segregation occurs in the distribution of refractory elements (Cr/W). The traditional gas atomization method (GA) often produces uneven alloy powder (containing Cr, W and other refractory elements) due to process limitations, affecting the quality and performance of the sample. The metal ingot required for induction melting furnace already contains a small amount of unmelted HEA powder particles. After ultra-short-term rapid melting and cooling process caused by centrifuge rotation, there is segregation of refractory elements in the final spherical powder [26–29]. This is why innovative powder production methods are needed to meet the needs for LPBF.

### 3.3. Thermal stability of SLM samples (powders)

By analyzing the endothermic peak and exothermic peak of

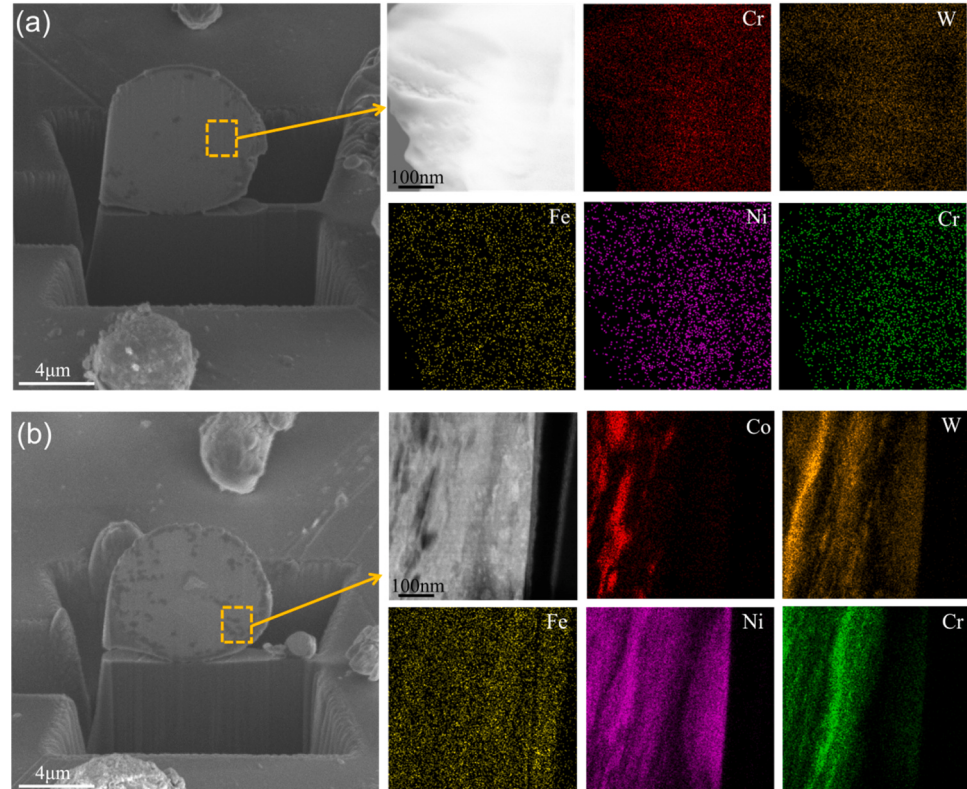


**Fig. 4.** Spherical cross-section morphology and EDS of spherical particles obtained by plasma high-temperature remelting and gas atomization, respectively.

differential scanning calorimeter (DSC) curve, some internal characteristics of SLM samples can be studied. Thus, the SLM sample was broken into alloy powder (20–40 μm) by crusher after additive manufacturing. It can be seen in **Fig. 5** that the DSC curve shows similar exothermic and endothermic processes. The powder ( $\text{Ni}_8\text{Cr}_4\text{Co}_4\text{Fe}_6\text{W}_2$ ) was spheroidized through the plasma nozzle, and the DSC curve showed an obvious exothermic peak in the temperature range of 100 °C to 600 °C, and the temperature span was large. Due to the plastic deformation of the particles in the mechanical alloying process, serious lattice distortion occurs. With the increase of temperature, the stored distortion energy in the alloy powder is gradually released [30]. The slope of the curve increases significantly from 700 °C to 900 °C, most likely due to heat absorption as the powder transforms into a face-centered cubic (FCC) structure. The curve has a small exothermic platform near 1000 °C, and finally a larger endothermic acromion between 1410 °C and 1450 °C. This shoulder is most likely caused by the melting of the alloy powder in the internal melting pool at this

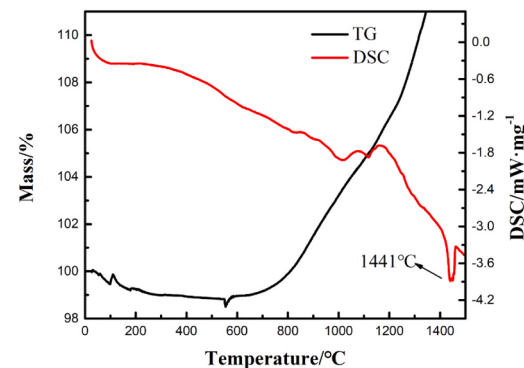


**Fig. 5.** DSC and TG of  $\text{Ni}_8\text{Cr}_4\text{Co}_4\text{Fe}_6\text{W}_2$  HEA powder.

temperature during the additive manufacturing process.

From the TG curve, the mass loss of  $\text{Ni}_8\text{Cr}_4\text{Co}_4\text{Fe}_6\text{W}_2$  curve is relatively large at the beginning. Under the action of temperature, the material will change with the increase of temperature, such as weight loss caused by water evaporation, loss of crystal water, low molecular weight volatilization, decomposition and oxidation of the material and other factors. With the increase of temperature, the change of thermogravimetric curve tends to be stable, and it has good oxidation resistance in the range of  $0\text{ }^\circ\text{C} \sim 750\text{ }^\circ\text{C}$ . The weight of the powder increases, indicating that the alloy powder loses its oxidation resistance at high temperatures. This is mainly due to the fact that the alloy powder is broken from SLM samples. The wet method is used to obtain powder after crushing. Some organic reagents (ethanol, etc.) may remain on the surface of the powder. When the temperature rises, ethanol breaks down into  $\text{O}_2$ .  $\text{O}_2$  reacts with the Fe element in the alloy powder to form  $\text{Fe}_2\text{O}_3$ . Due to the loose nature of  $\text{Fe}_2\text{O}_3$ , it is wrapped inside the oxide film, which makes the powder surface oxidized and heavier in mass.

#### 4. Results and discussion on SLM

##### 4.1. Phase structure

The XRD of GA-SLM and PHTR-SLM alloyed  $\text{Ni}_8\text{Cr}_4\text{Co}_4\text{Fe}_6\text{W}_2$  samples are shown in Fig. 6a. These two samples exhibit the same phase: a single face centered cubic (FCC) solid solution without a second phase. The lattice parameter of FCC phase is  $3.228\text{ \AA}$ , calculated by Debye-Scherer equation (The results were obtained by XRD software Jade 6.0). In addition, the lattice constant was calculated as  $0.426\text{ nm}$ . Furthermore, the angle of the (111) peaks of FCC phases in HEA shifts towards the left as the Ti is added, in accordance with the Bragg equation, which corresponds to the expansion of lattice constant. This indicates that W diffuses more fully under the PHTR process, causing more intense lattice distortion. Among the five elements (Ni, Cr, Co, W and Fe) in HEA, W has the largest atomic radius. It has a significant effect on the degree of lattice distortion and the change of lattice constants. In addition, the (111) diffraction peak intensity of PHTR-SLM alloy is largely enhanced compared with that of GA-SLM alloy. This is mainly due to crystallinity. In XRD, both crystallinity and grain size affect the diffraction peak intensity. It can be seen from the  $\text{Ni}_8\text{Cr}_4\text{Co}_4\text{Fe}_6\text{W}_2$  HEA that the influence of the former on the diffraction peak strength is greater than that of the latter [31,32]. The enthalpy of mixing between elements has a direct influence on the phase construction and stability of high entropy alloys, and is also an important reference for the composition design of high entropy alloys (see Table 5). It can be seen from Table 2 that the absolute enthalpy of mixing among Fe, Cr and Ni is small, indicating that these three elements can combine well to form a solid solution phase. The results show that FeNi alloys can form solid

**Table 5**

Enthalpy of mixing of each element atom pair /(kJ/mol) [33].

Mixing enthalpy	Ni	Cr	W	Fe	Co
Ni	-	-7	-3	-2	0
Cr	-7	-	1	-1	4
W	-3	1	-	16	16
Fe	-2	-1	0	-	-1
Co	0	4	-6	-1	-

solutions with FCC structure [33]. It can be seen from the enthalpy of mixing that W can also combine with Ni, Cr and Fe to form a solid solution phase.

Fig. 6b is the XRD pattern of HEA powder. It can be seen from the figure that the GA-SLM and PHTR-SLM three-phase peak are both a single FCC phase, consistent with the SLM sample. The laser energy density in the additive manufacturing process is very high, making some metastable powders with high energy storage release a lot of distortion energy in the form of heat and become stable. However, the PHTR powder has been melted at high temperature at the plasma nozzle (the nozzle temperature exceeds  $2000\text{ }^\circ\text{C}$ ). Thus, the prepared spherical powder has changed from metastable to be stable, making its phase structure consistent with the final SLM sample. Peak high intensity can reflect the relative intensity of diffraction peak, namely, the content of crystal phase. The peak surface of the high entropy alloy powder is smaller than that of the SLM sample, which means that the crystal phase content is also smaller.

##### 4.2. Microstructure and solidification mechanism

Fig. 7a shows the SEM image of PHTR-SLM alloy (cross section taken from the middle of the sample). Fig. 7b-f shows the distribution of elements captured by EDS. The additive manufacturing sample is prepared from PHTR powder after high temperature remelting. It can be seen from EDS that the components of Ni, Cr, W, Fe and Co are evenly distributed without segregation. In order to obtain a more detailed analysis of the microstructure and phase composition of  $\text{Ni}_8\text{Cr}_4\text{Co}_4\text{Fe}_6\text{W}_2$  HEA SLM alloy, TEM was used for microscopic characterization (Figs. 7g-i). The existence of solid solution and FCC structure is confirmed by diffraction pattern. Among them, Fig. 7g is a bright field image. The SAED diagram of Region 1 and Region 2 is shown in Fig. 7h and i. The crystal structure shown by the yellow dashed line is consistent with Fig. 7g. Zone 1 along the  $[-110]$  axis and Zone 2 along the  $[001]$  axis. It can be determined that the alloy phase of the  $\text{Ni}_8\text{Cr}_4\text{Co}_4\text{Fe}_6\text{W}_2$  high entropy alloy is FCC structure, which is consistent with the results of XRD characterization. TEM images show that the high entropy alloy under Ar protection is a single-phase FCC solid solution. The high energy

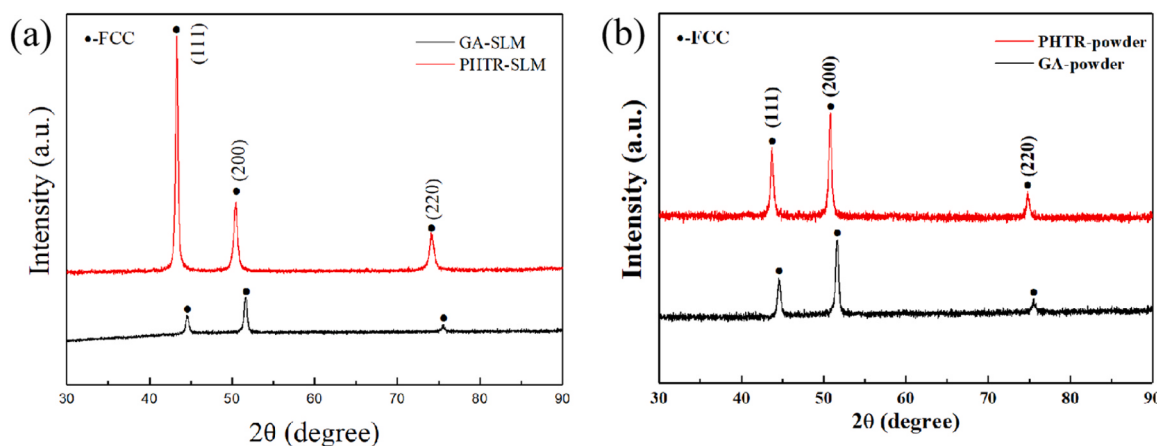
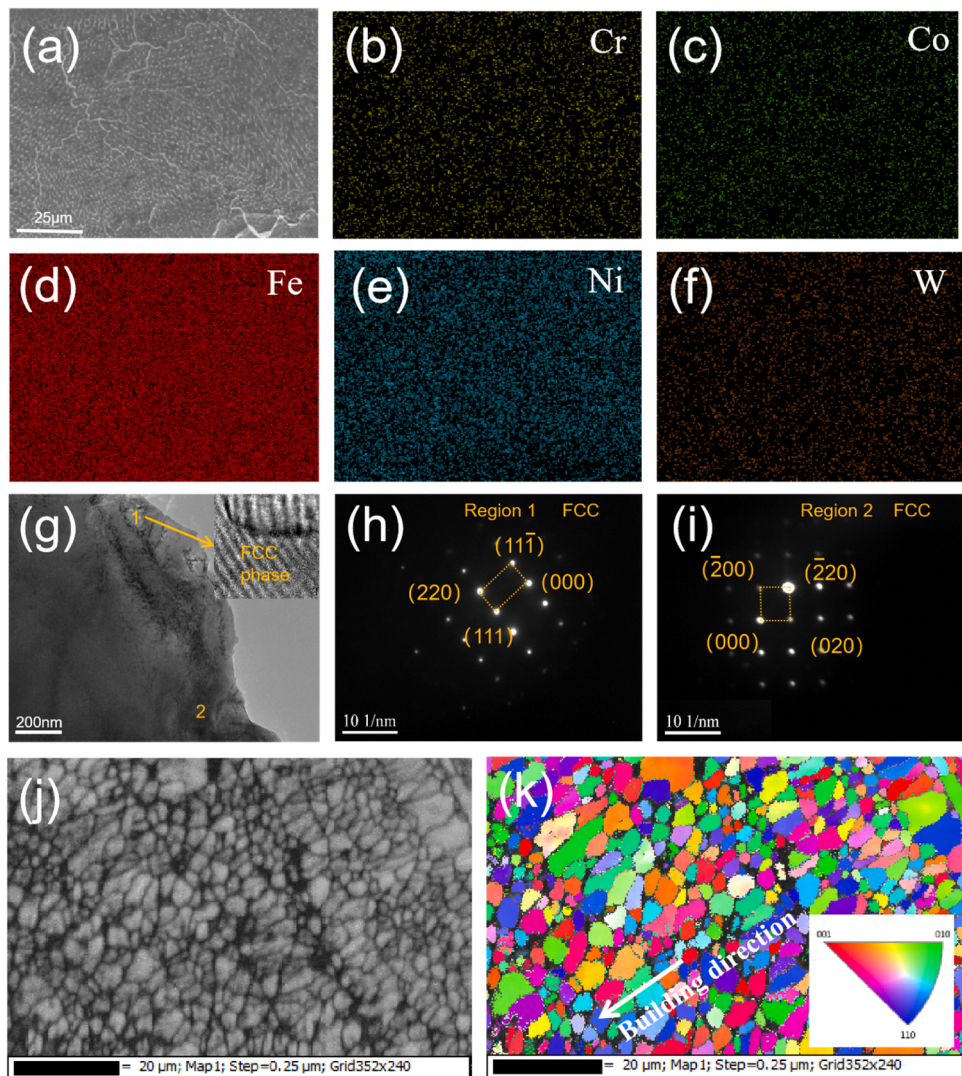


Fig. 6. (a) XRD of GA-SLM and PHTR-SLM; (b) XRD of GA-powder and PHTR-powder.



**Fig. 7.** (a) The SEM of PHTR-SLM, (b)-(f) Corresponding EDS images to the SEM, (g) The TEM bright field image of PHTR-SLM, (h)-(i) Corresponding to the SAED diagram, (j-k) The EBSD observation.

laser beam can be heated rapidly to increase the temperature, reduce the cooling rate, and improve the atomic migration ability

In addition, the middle section of the sample was observed with EBSD. Fig. 7j-k shows the typical microstructure of the mixed grain zone along the building direction where fine grains coexist with large grains. It can be seen from the figure that the grain is equiaxed and has no obvious texture. The microstructure development of molten pool is determined by solidification behavior [34]. In general, the additive manufacturing process experiences a fast melting and fast solidification process. During solidification, the grain growth direction tends to be perpendicular to the solid-liquid interface. At this time, the temperature gradient in this direction is the largest, and the driving force generated is also the largest [35].

In the process of SLM preparation of high-entropy alloy additive specimen, high energy laser irradiation and rapid cooling in a very short time will lead to the formation of fine grains, while the large temperature gradient and heat flow direction will promote the further formation of columnar crystals. In the process of SLM melting powder, there is a larger temperature gradient in the upper and lower edges of the melting pool, which will give priority to rapid solidification. When the laser scans the next layer of powder, the heat will rapidly diffuse and remelt the solidified surface, and the precipitation evenly distributed on the FCC solid solution in the remelt zone will provide new heterogenous

nucleation points, and the alloy will quickly nucleate into equiaxed crystals. At the same time, the original equiaxed grains will show ductile growth characteristics along the forming mode and penetrate multiple forming layers. In addition, the middle and top structures are mainly composed of fine equiaxed crystals. This is due to the fast scanning speed and short solidification time of high entropy alloy forming in the process of high energy laser, the grain nucleation is less than the growth, and the growth becomes a fine structure, thus affecting the alloy properties.

#### 4.3. Effect of strain rate sensitivity index on hardness

The nanoindentation load-displacement curves of Ni<sub>8</sub>Cr<sub>4</sub>Co<sub>4</sub>Fe<sub>6</sub>W<sub>2</sub> high-entropy alloy samples with the same composition in two different powder processing processes are shown in Fig. 8. The given pressing depth of the block sample is 1500 nm, as shown in Fig. 8a-b. It can be seen that the applied load required by the GA-SLM sample is smaller than that required by PHTR-SLM. With the increase of rolling amount, the applied load reaching the same pressing depth shows an increasing trend, indicating that the corresponding hardness value has the same changing trend. There is no jump in the load-displacement curves of all samples, indicating that the single-phase face-centered cubic high-entropy alloy prepared has uniform structure and no obvious internal defects.

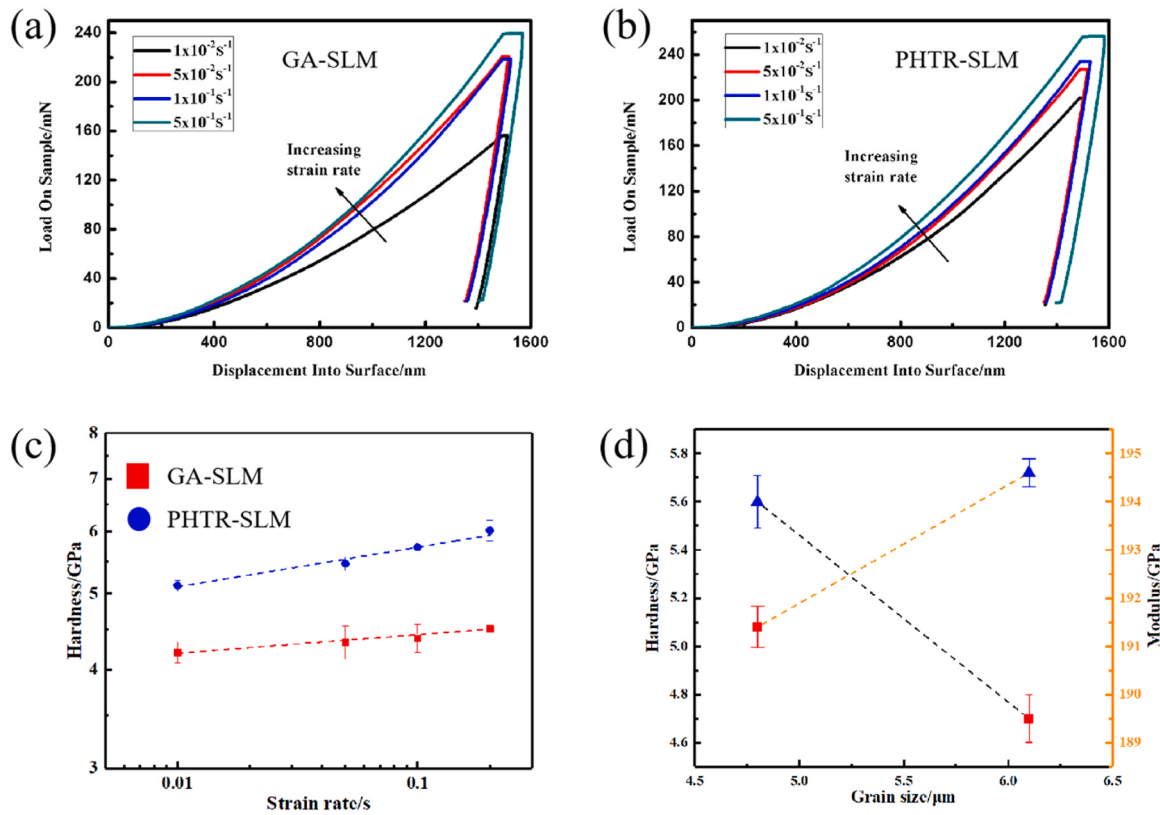


**Fig. 8.** (a)-(b) Load-displacement curve for nanoindentation hardness testing, (c) The change of hardness of high entropy alloy with loading strain rate, (d) Hardness and elastic modulus of Ni<sub>8</sub>Cr<sub>4</sub>Co<sub>4</sub>Fe<sub>6</sub>W<sub>2</sub> HEA with different grain sizes.

Generally, the strain rate sensitivity index  $m$ , where strain and temperature are the same during deformation, is only a function of the strain rate change corresponding to hardness  $H$  [36].

$$m = \frac{\partial \ln H}{\partial \ln \dot{\epsilon}} \quad (1)$$

Where, the loaded strain rate  $\dot{\epsilon}$  is generally obtained according to the following formula:

$$\dot{\epsilon} = \frac{1}{h} \frac{\partial h}{\partial t} \quad (2)$$

Where:  $h$  represents instantaneous pressing depth /nm;  $t$  means time /s.

Different deformation mechanisms of metal materials correspond to different strain rate sensitivity  $m$ . Its value usually fluctuates between 0 and 1. A high  $m$  value indicates that the material has a strong ability to resist local deformation and can produce uniform plastic deformation. For traditional metal alloys, the strengthening mechanism of coarse-grained materials is mainly dislocation strengthening. It is not sensitive to strain rate, and  $m$  values are usually between 0.125 and 0.333. The  $m$  value of the grain boundary and lattice diffusion mechanism is generally about 1 [37].

In order to show the relationship between hardness and strain rate, Fig. 8c shows the hardness trend of single-phase Ni<sub>8</sub>Cr<sub>4</sub>Co<sub>4</sub>Fe<sub>6</sub>W<sub>2</sub> high-entropy SLM with loading rate under different powder preparation processes. It can be seen that the hardness of Ni<sub>8</sub>Cr<sub>4</sub>Co<sub>4</sub>Fe<sub>6</sub>W<sub>2</sub> high-entropy alloy increases with the decrease of grain size under the same loading rate. For the same sample, the hardness increases with the increase of the loading strain rate, indicating that Ni<sub>8</sub>Cr<sub>4</sub>Co<sub>4</sub>Fe<sub>6</sub>W<sub>2</sub> high-entropy alloy with FCC crystal structure has a positive strength (hardness) strain rate sensitivity, which is consistent with traditional face-centered cubic metals. The  $m$  values of GA-SLM and PHTR-SLM samples are 0.030 and 0.027, respectively, by linear fitting of hardness

variation trend with loading strain rate. The hardness value of the range with stable change of hardness value was obtained. The hardness values of the bulk samples and the nanocrystals were obtained from the depth of 800–1200 nm and from the depth of 80–160 nm. Fig. 8d shows the results of nanoindentation hardness and elastic modulus of Ni<sub>8</sub>Cr<sub>4</sub>Co<sub>4</sub>Fe<sub>6</sub>W<sub>2</sub> high-entropy alloy samples obtained by different powder preparation processes. The hardness of Ni<sub>8</sub>Cr<sub>4</sub>Co<sub>4</sub>Fe<sub>6</sub>W<sub>2</sub> high-entropy alloy shows a trend of continuous increase with the decrease of grain size. In addition, the elastic modulus does not change much (PHTR-SLM is 193 Gpa and GA-SLM is 189 Gpa). It can be seen that the hardness and elasticity are positively correlated with the same grain size. It is not sensitive to the organization of the material, such as heat treatment, cold plastic deformation has a small impact on it, but it will fluctuate about 5 % in the heat treatment state of the material and cold plastic deformation.

The shear transition zone (STZ volume) of the alloy with larger elastic modulus is smaller and the depth is shallower. The elastic modulus of high entropy alloys is often considered to be related to the bond energy [38,39]. At room temperature, the high entropy alloy has plastic flow through the activation and combination of STZ to form a localized shear band. Therefore, the greater the elastic modulus, the greater the overall bond energy of the alloy. The higher the activation energy required for the atoms that make up STZ, the more difficult it becomes to activate STZ [39]. The smaller the volume of STZ produced, the less the plastic flow of amorphous alloy occurs when the needle tip is inserted, and the formation of localized shear band is hindered. The final performance is that the shallower the depth of the scratch, the better the scratch resistance and the stronger the wear resistance.

The absolute value of  $m$  in metal alloys is closely related to the plastic deformation mechanism of metal crystal materials. For face-centered cubic metals,  $m$  tends to 0 if the dislocation-related mechanism dominates, and  $m$  tends to 1 if the grain-boundary related mechanism dominates. Therefore, dislocation deformation at room temperature is the

main plastic deformation mechanism in large grain size alloys due to the very low volume fraction of the inner grain boundaries. Therefore, the  $m$  value of traditional face-centered cubic metal coarse crystal is small.

#### 4.4. Wear resistance and stress state analysis in friction process

**Fig. 9a** shows the wear weight loss intensity of  $\text{Ni}_8\text{Cr}_4\text{Co}_4\text{Fe}_6\text{W}_2$  HEA sample on wear samples. PHRT-SLM has less wear than GA-SLM. This is because higher hardness may lead to increased wear resistance of HEA alloys [39–42]. **Fig. 9b** depicts the relationship of the coefficient of friction over time. With the progress of friction process, the actual contact area is increasing, resulting in a sharp increase in friction coefficient. After entering the stable wear zone, the stable friction coefficient of PHRTR-SLM is about 0.47, and the average stable friction coefficient of GA-SLM is 0.52. For metal materials, the smaller the friction coefficient, the more stable, the better the wear resistance. SLM technology includes a rapid solidification process. The nucleation rate of alloy increases rapidly, resulting in the rapid decline in the grain size. The atom diffusion is slow in fast solidification and the growth of crystal nucleus is limited. At last, the fine crystal is obtained and the fine crystal strengthening is formed as well. This fine-grained strengthening mechanism increases the wear resistance of the SLM samples [25]. The two different value in the wear resistance is mainly attributed to the particle size of the powders used in additive manufacturing, affecting the grain size. Thus, the final results of fine grain strengthening show different effects as well.

**Fig. 9c-d** represent the SEM of the wear surface of the wear sample. As for PHRT-SLM (**Fig. 10c**), no cracks or spalling are observed on the worn surface. The wear surface of PHRT-SLM has almost no wedge formation, which is a typical micro-cutting mechanism. What's more, it forms a large number of nano-oxide inclusions at the grain boundary, having a very high microhardness and resists the shear force generated by friction with the friction pair during wear. Some unwedged grooves appeared on the wear surfaces of GA-SLM sample in **Fig. 8d**. A small number of wedge grooves appear on the surface of the specimen and the fragmentation and delamination of wedge grooves can be seen as well. This is due to an external force (contact load) acting on the metal surface

during wear. Stress concentration usually occurs in certain areas where there are (groove-based) nicks. It indicates that the wear mechanism of GA-SLM. sample is a mixture of micro-tillage and micro-cutting. Under a load of 15 N, **Fig. 10e-f** show the 3D morphology of wear samples detected by 3D laser scanning microscope. PHTR method makes the wear degree of the wear sample appear parallel groove since it stimulates the fine-grained strengthening mechanism [41,42]. The results indicates the process changing on the main wear mechanism: from micro-plowing to micro-cutting and micro-plowing. In addition, it can be seen from the three-dimensional surface topography that the groove width decreases gradually with grains decrease.

In order to study the influence of contact load on the stress state of high entropy alloy, the friction and wear testing machine used in this experiment is to apply a load to the ball. The ball is subjected to reciprocating friction on the surface of the prepared sample. At the beginning of the experiment, the small balls touch the  $\text{Ni}_8\text{Cr}_4\text{Co}_4\text{Fe}_6\text{W}_2$  high entropy alloy surface with a certain load, which is similar to the Hertz contact. The Hertz contact theory is derived from the static contact conditions of completely elastic bodies. This theory is used to solve the elastic deformation and stress field of surface contact, and is the basic theory of friction and wear research [43].

The distribution of the Mises stress along the center line of the  $\text{Ni}_8\text{Cr}_4\text{Co}_4\text{Fe}_6\text{W}_2$  PHTR-SLM section is shown in **Fig. 10a**. The maximum value of the Mises stress is located at the subsurface, and the value of the Mises stress increases with the increase of the load. However, due to the plastic deformation of the subsurface, the stress state of the subsurface region is changed and the stress value is reduced. For example, when the load was 15 N, the maximum Mises stress calculated according to Hertz contact theory was 1610 MPa, and the maximum Mises stress after plastic deformation was 1125 MPa. **Fig. 10b** shows that the maximum equivalent plastic strain value is also located at the sub-surface, and the equivalent plastic strain value increases with the increase of load. Under 15 N load, the equivalent plastic strain value is 0.4 %. Due to the presence of plastic strain, the contact area between the pellets and  $\text{Ni}_8\text{Cr}_4\text{Co}_4\text{Fe}_6\text{W}_2$  PHTR-SLM presents a concave feature, which reduces the stress value of the contact center between the pellets and  $\text{Ni}_8\text{Cr}_4\text{Co}_4\text{Fe}_6\text{W}_2$ . **Fig. 10c** shows the curve of increasing contact stress with load at

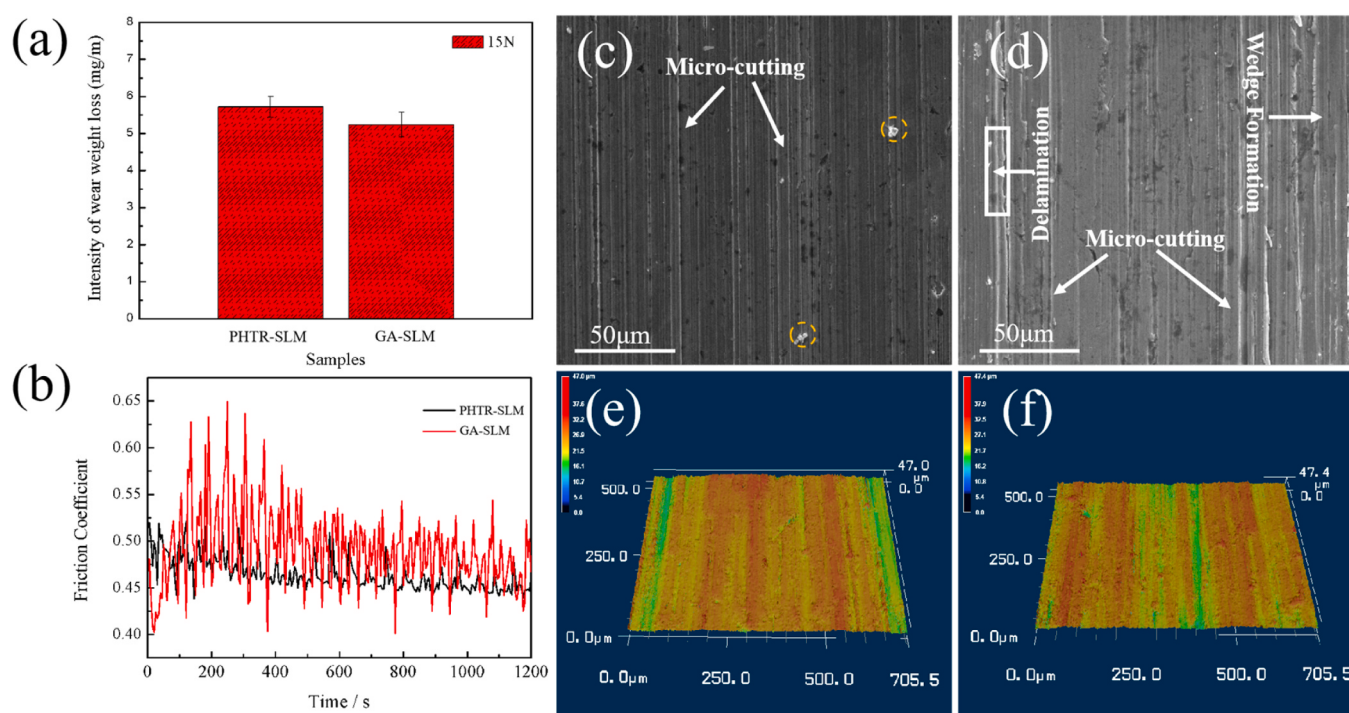


**Fig. 9.** (a) Wear loss, (b) Friction coefficient, (c) SEM of PHTR-SLM (d) SEM of GA-SLM, (e) 3D profiles of PHTR-SLM, (f) 3D profiles of GA-SLM.

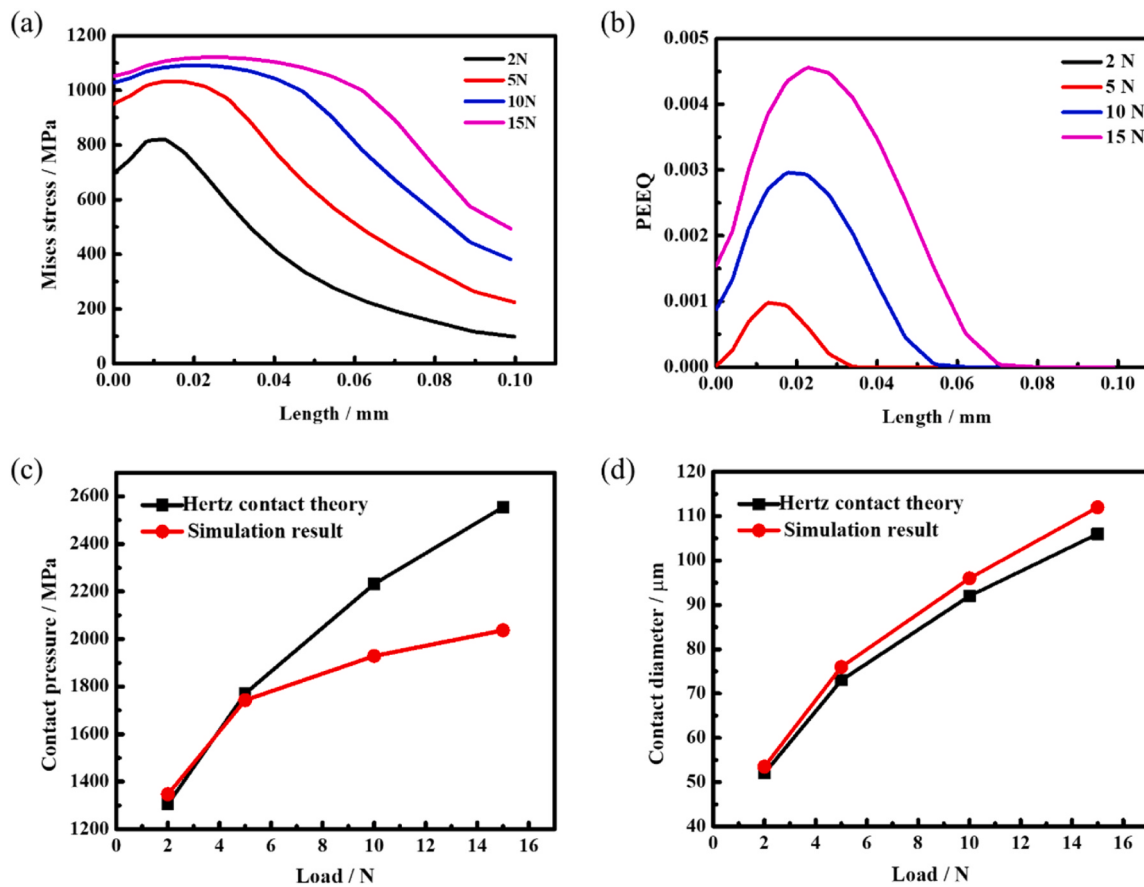


**Fig. 10.** Stress of cross-section and surface, a) Mises stress distribution of cross-section centerline, b) PEEQ of cross-section centerline, c) Hertz theoretical value and simulation value of contact pressure, d) Hertz theoretical value and simulation value of contact area.

the contact center point confirming the appeal inference. Under 2 N and 5 N loads, the plastic deformation is not obvious, so the simulated contact pressure is not different from the theoretical calculation. With the increase of load, the plastic deformation increases significantly. When the load is 15 N, the simulated value of the contact stress decreases by 23 % compared with the theoretical value. Fig. 10d shows the difference between the theoretical and simulated values of Herzt contact at the contact radius. According to the simulation results, the contact radius increases with the increase of plastic deformation in addition to the reduction of contact pressure. The increase of contact radius is most obvious at 15 N load. The increase of the contact radius can also reduce the value of the contact stress.

#### 4.5. Mechanical properties

Fig. 11 shows the room temperature mechanical properties of GA-SLM and PHTR-SLM alloys of horizontal tensile samples under Ar protection in the direction horizontally perpendicular to the laser scanning direction (Y). In order to control variables and eliminate experimental errors, the average particle size of GA and PHTR powders used by the authors is almost the same. Tensile samples were prepared according to the Tensile Test Standard for Metallic Materials (GB/T228–2002). It is clear that the average elongation ( $\varepsilon$ ) of the PHTR-SLM sample and yield strength (YS) are higher than that of GA-SLM sample. The  $\varepsilon$  (PHTR) is 14.8 % higher than that of GA(10.6 %). In PHTR-SLM, Its yield strength (YS) is 789 MPa and UTS is tested as 1062 MPa. At the same time, the YS and UTS of the GA-SLM sample are 590 MPa and 843 MPa, respectively. Compared with GA method, the elongation, YS and UTS of PHTR-SLM alloy have increased by 39.6 %, 33.7 % and 25.9 %, respectively.

The strength of alloy materials can be improved by the presence of

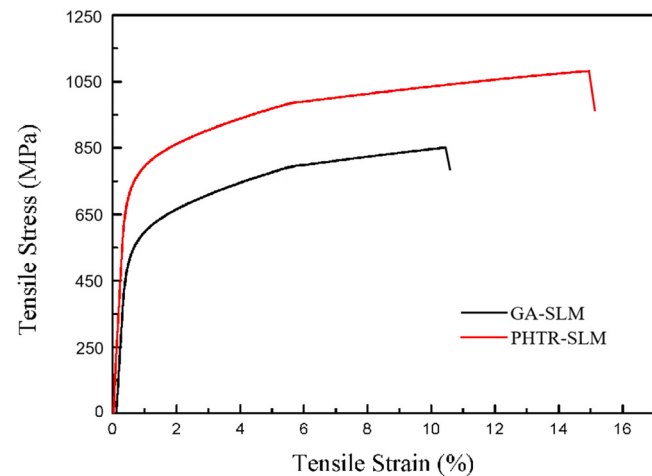


**Fig. 11.** The mechanical properties of GA-SLM and PHTR-SLM alloy.

interstitial solutes and alternative solutes in high entropy alloys [44]. Interstitial atoms or substitution atoms (Fe, Cr, W, Co,) can enter the lattice in large numbers, eventually leading to interstitial solid solution strengthening. In metal materials science, fine grains provide grain boundaries with a higher volume fraction, preventing dislocation from moving during deformation. The nucleation rate of the alloy increases sharply in the SLM process [45]. This can lead to a rapid reduction in grain size formation, resulting in finer grains and increasing the strength of the alloy material. The Hall-Page equation describes the effect of grain size on mechanical properties as follows:

$$d = \left(\frac{V}{I}\right)^{\frac{1}{3}} \quad (3)$$

Where,  $I$  is nucleation rate;  $V$  represents grain growth rate and  $d$  means grain size.

In the SLM additive specimen, it can be observed that the structure is mainly composed of equiaxial crystals. The size of these grains remains between 500 nm and 5000 nm, which is much smaller than the size of the casting (generally between tens to hundreds of microns). As a result, the SLM additive alloy was fine-grained strengthened, which improved the plasticity.

When laser cladding is performed on the bottom of the additive specimen, the grains precipitate and cool rapidly, so the grain size in the bottom region is smaller than that in other regions. Since the cooling condition of the middle part is worse than that of the bottom part, the grain size of the middle layer is larger than that of other regions. The grain size of the top layer is smaller than that of the middle layer because the middle layer is not affected by subsequent heating. In view of this, it is necessary to accumulate heat on the previously deposited layer and reheat the next layer in order to obtain a better equiaxed additive specimen.

In addition, our work has been compared with the mechanical properties of other high entropy alloys with similar compositions (Fig. 12 and Table 6). It is not difficult to find that the three data (elongation ( $\epsilon$ ), yield strength (YS) and ultimate tensile strength (UTS) in this work are all higher than those in previous studies [46–48]. The selected studies all contain refractory elements. This work is also compared by different processes with the same composition. It is also proved that the uniformity of refractory elements has a great influence on the mechanical properties of HEAs. For alloys containing refractory elements, the spherical powders obtained by common processes (PREP, GA) have the problem of uneven composition. There is component segregation in the molded parts prepared by additive manufacturing, resulting in uneven local distribution of stress in the molded parts during high temperature service. And it is easy to appear local deformation and cause cracking. It restricts the large-scale application of additive manufacturing metals in the field of preparing high-temperature

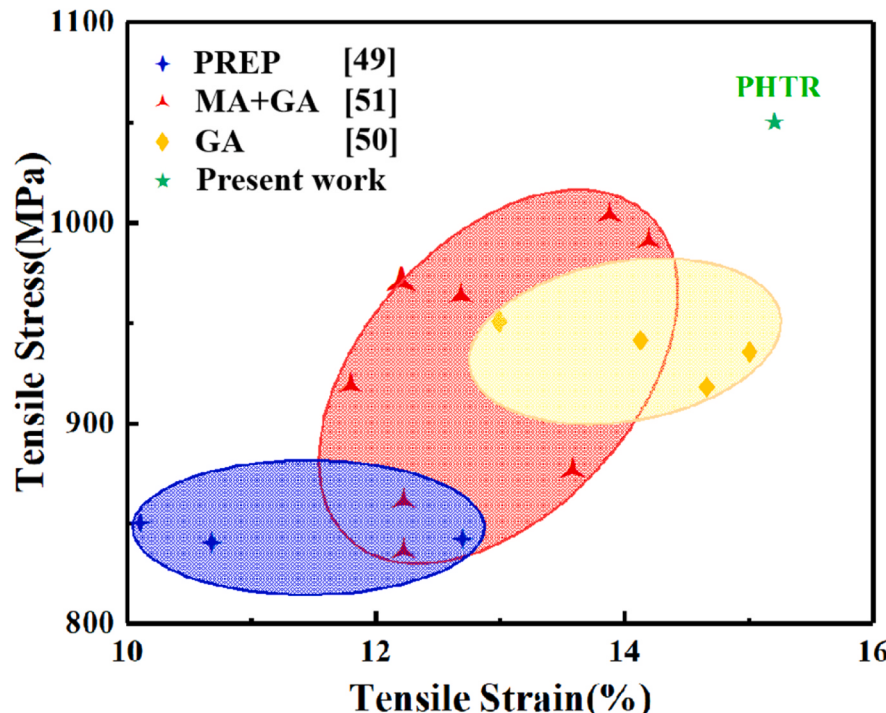
**Table 6**  
Mechanical properties of different HEA alloys at room temperature.

Name	Method	$\sigma_y/\text{MPa}$	$\sigma_{UTS}/\text{MPa}$	$\epsilon/\%$
CoCr <sub>2.5</sub> FeNi <sub>2</sub> TiW <sub>0.5</sub> [46]	PREP	581	893	9.9
Ni6Cr4WFe9Ti [47]	GA	742	972	12.2
Ni6Cr4WFe9Ti [48]	MA+GA	710	983	12.7
Present work	GA	590	843	10.6
Present work	PHTR	789	1062	14.8

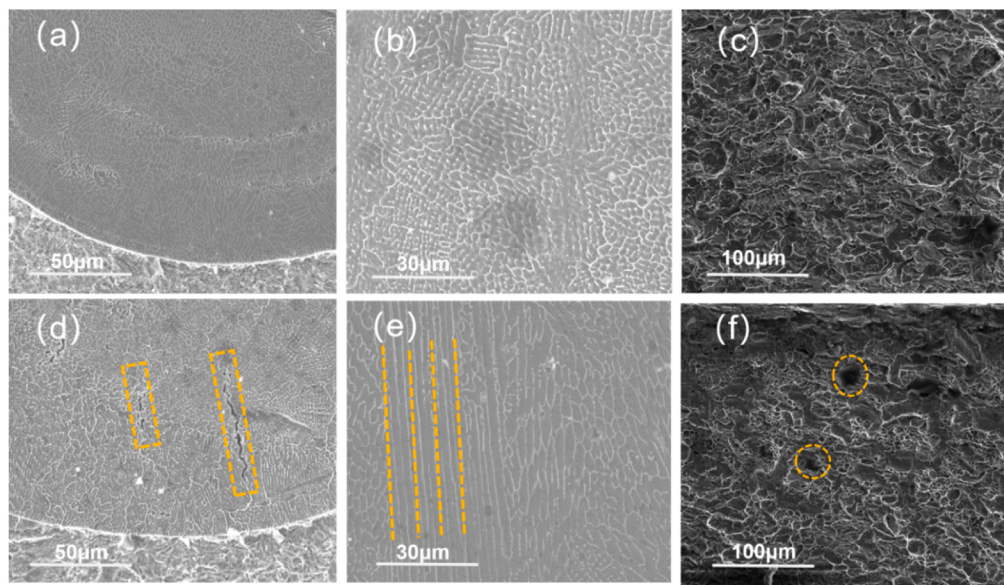
resistant materials.

Fig. 13a and d show the micromorphologies of spherical powders prepared by different processes (a: PHTR-SLM; b: GA-SLM). It is clear that GA-SLM has cracks (Fig. 13d, yellow circle). Intrachrysalline segregation can result in uneven grain composition and eventually different grain types: for PHTR, additive manufacturing results in equiaxed crystals (Fig. 13b). For GA-SLM, component segregation results in a mixture of equiaxed and columnar crystals (Fig. 13e). This ultimately leads to a decrease in the mechanical properties of the alloy, especially the ductility and toughness [49]. The fracture morphology of Ni<sub>8</sub>Cr<sub>4</sub>Co<sub>4</sub>Fe<sub>6</sub>W<sub>2</sub> high-entropy alloy prepared by additive manufacturing process is shown in Fig. 13c (PHTR-SLM) and Fig. 13f (GA-SLM), respectively. High density tear dimples were present in the fracture of SLM specimen (Fig. 13c). This is a typical ductile fracture, in line with FCC structural characteristics. Some relatively flat areas can be observed on the surface of Fig. 13f, and there are small pores in the area. Due to the high degree of supercooling of the liquid metal, gas is discharged from the molten pool during the melting process. The viscosity of the molten liquid is significantly reduced, and the liquid metal cannot completely enter the pores, and eventually the pores are formed.

In the preparation of high-entropy alloy additive specimens by SLM, the alloyed powders were irradiated by laser to rapidly heat and melt to form a molten pool. When the laser scanning beam scans other areas, the molten pool will quickly solidify under the extreme cooling rate. In this process, the SLM process is characterized by rapid solidification, resulting in a very small size of the alloy additive specimen and a supersaturated FCC solid solution. Under different preparation processes of alloy powder, the grain size and tensile fracture distribution



**Fig. 12.** The mechanical properties of different HEAs.



**Fig. 13.** The fracture surfaces by different manufacturing processes (a)-(b) PHTR-SLM, (c)-(d) GA-SLM.

characteristics of HEA alloy are different, which affect the fracture behavior of HEA alloy. In addition, there is a large temperature gradient when the alloy melts and solidifies, and cracks, spheroidization and other defects occur during the layer by layer forming process, which seriously affects the microstructure and properties of the additive specimen.

## 5. Conclusion

In this paper, spherical high entropy alloy powders were prepared by a new technology, aiming at composition uniformity. Thus, The high entropy alloy spherical powders ( $\text{Ni}_8\text{Cr}_4\text{Co}_4\text{Fe}_6\text{W}_2$ ) prepared by the method were used to print the forming parts by additive manufacturing. The evaluation includes the preparation of 3D forming parts with the same chemical composition by conventional GA processes as a reference. The ability to produce refractory HEAs through PHTR method will make it possible to manufacture complex geometry shapes in high temperature service environment (such as aviation engine blades) with bright application potential at a reasonable cost. The conclusions were made as follows:

- The HEA powder obtained by PHTR method can homogenize the internal composition. The rapid solidification characteristics of SLM process make the alloy specimens have extremely small size and obtain single FCC solid solution.
- The strain rate sensitivity index  $m$  of GA-SLM and PHTR-SLM samples were 0.030 and 0.027, respectively. The hardness of  $\text{Ni}_8\text{Cr}_4\text{Co}_4\text{Fe}_6\text{W}_2$  HEA showed a trend of continuous increase with the decrease of grain size.
- The simulated value of the contact stress decreased by 23% compared with the theoretical value. The contact radius increased with the increase of plastic deformation in addition to the reduction of contact pressure.
- The average elongation ( $\epsilon$ ), yield strength (YS) and ultimate tensile strength (UTS) samples were 14.8 %, 798 MPa and 1062 MPa, respectively by the PHTR-SLM.
- The sample value of the elongation ( $\epsilon$ ), YS and UTS on  $\text{Ni}_8\text{Cr}_4\text{Co}_4\text{Fe}_6\text{W}_2$  (PHTR-SLM) has increased by 39.6 %, 33.7 % and 25.9 %, respectively in additive manufacturing, compared to GA-SLM.

## CRediT authorship contribution statement

**Peng Zhang:** Investigation. **Pengcheng Zhang:** Methodology. **Jiayu He:** Investigation, Data curation. **Hongjing Wu:** Supervision, Software. **Zhen Gu:** Writing – original draft, Resources, Funding acquisition, Conceptualization. **Danli Zhang:** Investigation. **L L Xiao:** Supervision. **Shengqi Xi:** Writing – review & editing, Visualization. **Yuanbin Qin:** Investigation.

## Declaration of Competing Interest

The authors declare that they have known no competing financial interests or personal relationships that could have appeared to influence the work reported in this paper.

## Data availability

No data was used for the research described in the article.

## Acknowledgments

This work was supported by National Natural Science Foundation of China (Grant No. 52201138). We also thank the Instrument Analysis Center of Xi'an Jiaotong University for providing characterization analysis. Zhen Gu and Jiayu He are co-first authors of the article.

## References

- [1] J. Martin, B. Yahata, J. Hundley, et al., 3D printing of high-strength aluminum alloys. *Nature* 549 (7672) (2017) 365–369.
- [2] S. Singh, N. Wandlerka, B.S. Murty, U. Glatzel, J. Banhart, Decomposition in multicomponent AlCoCrCuFeNi high-entropy alloy, *Acta Mater.* 59 (1) (2011) 182–190.
- [3] Y.F. Ye, C.T. Liu, Y. Yang, A geometric model for intrinsic residual strain and phase stability in high entropy alloys, *Acta Mater.* 94 (1) (2015) 152–161.
- [4] Y.L. Wang, C.F. Sun, Z. Gu, et al., Effect of C content on microstructure and properties of (FeCoCrNi)88-xMo8WNb3Cx high entropy alloys by additive manufacturing, *Dev. Appl. Mater.* 39 (1) (2024) 14–22. +46.
- [5] J. Li, N. Deng, P. Wu, et al., Elaborating the Cu-network structured of the W-Cu composites by sintering intermittently electroplated core-shell powders, *J. Alloy. Compd.* 770 (2019) 405–410.
- [6] T. Borkar, B. Gwalani, D. Choudhuri, C.V. Mikler, C.J. Yannetta, X. Chen, R. V. Ramanujan, M.J. Styles, M.A. Gibson, R. Banerjee, A combinatorial assessment of  $\text{Al}_x\text{Cr}_x\text{Cu}_x\text{Fe}_x\text{Ni}_2$  ( $0 < x < 1.5$ ) complex concentrated alloys: microstructure, microhardness, and magnetic properties, *Acta Mater.* 116 (2016) 63–76.

- [7] D.B. Miracle, M.-H. Tsai, O.N. Senkov, et al., Refractory high entropy superalloys (RSAs), *Scr. Mater.* 187 (2020) 445–452.
- [8] Y. Mae, Anthropic principle observed in the material properties of Fe[J], *J. Mater. Sci. Res.* 6 (3) (2017) 11–19.
- [9] Y.F. Juan, J. Li, Y.Q. Jiang, W.L. Jia, Z.J. Lu, Modified criterions for phase prediction in the multi-component laser-clad coatings and investigations into microstructural evolution/wear resistance of FeCrCoNiAlMo<sub>x</sub> laser-clad coatings, *Appl. Surf. Sci.* 465 (2019) 700–714.
- [10] Y. Zhu, J. Narayan, J. Hirth, et al., Formation of single and multiple deformation twins in nanocrystalline fcc metals, *Acta Mater.* 57 (13) (2009) 3763–3770.
- [11] D. Debroy, H. Wei, J. Zuback, et al., Additive manufacturing of metallic components Process, structure and properties, *Prog. Mater. Sci.* 92 (2018) 112–224.
- [12] Q.Y. Chen, J. Yin, X.Y. Chen, et al., Microstructure and microhardness of interfaces of high thermal conductivity Ag-Cu dissimilar metals fabricated by laser powder bed fusion additive manufacturing, *Dev. Appl. Mater.* 39 (1) (2024) 1–13.
- [13] G. Chen, S. Zhao, P. Tan, J. Wang, C. Xiang, H. Tang, A comparative study of Ti-6Al-4V powders for additive manufacturing by gas atomization, plasma rotating electrode process and plasma atomization, *Powder Technol.* 333 (2018) 38–46.
- [14] Q. Wei, S. Cheng, K. Ramesh, et al., Effect of nanocrystalline and ultrafine grain sizes on the strain rate sensitivity and activation volume: fcc versus bcc metals[J], *Mater. Sci. Eng.* 381 (1-2) (2004) 71–79.
- [15] Y.M. Wang, A.V. Hamza, E. Ma, Temperature-dependent strain rate sensitivity and activation volume of nanocrystalline Ni, *Acta Mater.* 54 (10) (2006) 2715–2726.
- [16] Z. Tan, Z. Zhou, X. Wu, et al., In situ synthesis of spherical W-Mo alloy powder for additive manufacturing by spray granulation combined with thermal plasma spheroidization, *Int. J. Refract. Met. Hard Mater.* 95 (2021) 1–9, 105460.
- [17] X. Chang, M. Zeng, K. Liu, L. Fu, *Adv. Mater.* 32 (2020) e1907226.
- [18] C. Varvenne, G.P.M. Leyson, M. Ghazisaeidi, W.A. Curtin, *Acta Mater.* 124 (2017) 660–683.
- [19] W.G. Nohring, W.A. Curtin, *Scr. Mater.* 187 (2020) 210–215.
- [20] L.R. Owen, N.G. Jones, *Scr. Mater.* 187 (2020) 428–433.
- [21] M. Kajihara, Settling velocity and porosity of large suspended particle, *J. Oceanogr. Soc. Jpn.* 27 (4) (1971) 158–162.
- [22] R. Mei, R.J. Adrian, T.J. Hanratty, Particle dispersion in isotropic turbulence under stokes drag and basset force with gravitational settling, *J. Fluid Mech.* 225 (1991) 481–495.
- [23] H. Liu, R.H. Rangel, E.J. Lavernie, Modeling of droplet-gas interactions in spray atomization of Ta-2.5W alloy, *Mater. Sci. Eng. A* 191 (1-2) (1995) 171–184.
- [24] Gu Z., Xi S., Mao P., et al. Microstructure and wear behavior of mechanically alloyed powder Al x Mo 0.5 NbFeTiMn 2 high entropy alloy coating formed by laser cladding[J]. *Surface and Coatings Technology*, 401.
- [25] Z. Gu, S. Xi, C. Sun, Microstructure and properties of laser cladding and CoCr2.5FeNi2Ti high-entropy alloy composite coatings, *J. Alloy. Compd.* (2019). Article 152986.
- [26] Z. Tan, Z. Zhou, X. Wu, et al., In situ synthesis of spherical W-Mo alloy powder for additive manufacturing by spray granulation combined with thermal plasma spheroidization, *Int. J. Refract. Met. Hard Mater.* 95 (2021) 1–9, 105460.
- [27] G. Sun, K. Wang, R. Zhou, et al., effect of different heat treatment temperatures on the laser cladded M3:2 high-speed steel, *Mater. Des.* 65 (2015) 606–616.
- [28] P. Mercelis, J. Kruth, Residual stresses in selective laser sintering and selective laser melting, *Rapid Prototyp. J.* 12 (2006) 254–256.
- [29] Z.B. Cai, X.F. Cui, G. Jin, Z. Liu, W. Zheng, Y. Li, L.Q. Wang, Microstructure and thermal stability of a NiCrCoTiV-Al high-entropy alloy coating by laser surface alloying, *Met. Mater. Int.* 23 (2017) 1012–1018.
- [30] S. Varalakshmi, M. Kamaraj, B.S. Murty, Synthesis and characterization of nanocrystalline AlFeTiCrZnCu high entropy solid solution by mechanical alloying, *J. Alloy. Compd.* 460 (1-2) (2008) 253–257.
- [31] A. Ahmad, H.A. Khonakdar, C. Scheffler, et al., Poly(ethylene succinate)/single-walled carbon nanotube composites: a study on crystallization, *Polym. Bull.* 70 (12) (2013) 3463–3474.
- [32] H. Billetter, U. Ruschewitz, Structural phase transitions in Ag2Se (naumannite), *Z. Anorg. Allg. Chem.* 634 (2008) 241–246.
- [33] A. Takeuchi, A. Inoue, Classification of bulk metallic glasses by atomic size difference, heat of mixing and period of constituent elements and its application to characterization of the main alloying element, *Mater. Trans.* 46 (12) (2005) 2817–2829.
- [34] Hojjat Samaei Baghbadorani, Kermanpur, Najafizadeh Ahmad, Peiman Behjati, Mohammad Moallemi, Influence of Nb-microalloying on the formation of nano/ultrafine-grained microstructure and mechanical properties during martensite reversion process in a 201-type austenitic stainless steel, *Metall. Mater. Trans. A* 46 (8) (2015) 3406–3413.
- [35] E. Welsch, D. Ponge, S.M. Hafez Haghighat, S. Sandlobes, P. Choi, Strain hardening by dynamic slip band refinement in a high-Mn lightweight steel, *Acta Mater.* 116 (2016) 188–199.
- [36] J.R. Trelewicz, C.A. Schuh, The Hall-Petch breakdown in nanocrystalline metals: A crossover to glass like deformation, *Acta Mater.* 55 (17) (2007) 5948–5958.
- [37] I.A. Ovid'ko, R.Z. Valiev, Y.T. Zhu, Review on superior strength and enhanced ductility of metallic nanomaterials, *Prog. Mater. Sci.* 94 (2018) 462–540.
- [38] Zhao W., Li G., Wang Y., et al. Atomic bond proportions and relations to physical properties in metallic glasses[J]. *Materials & Design* (1980–2015), 2015, 65: 1048–1052.
- [39] W. Zhao, J. Cheng, S. Feng, et al., Intrinsic correlation between elastic modulus and atomic bond stiffness in metallic glasses, *Mater. Lett.* 175 (2016) 227–230.
- [40] D.W. Yi, J.D. Xing, S.Q. Ma, H.G. Fu, Y.F. Li, W. Chen, J.B. Yan, J.J. Zhang, R. R. Zhang, Investigations on microstructures and two-body abrasive wear behavior of Fe-B cast alloy, *Tribol. Lett.* 45 (2012) 427–435.
- [41] Y.X. Jian, Z.F. Huang, J.D. Xing, B.C. Zheng, L. Sun, Y.Z. Liu, Y.M. Liu, Effect of improving Fe2B toughness by chromium addition on the two-body abrasive wear behavior of Fe-3.0 wt% B cast alloy, *Tribol. Int.* 101 (2016) 331–339.
- [42] Y.X. Jian, Z.F. Huang, J.D. Xing, X.Z. Guo, Y. Wang, Z. Lv, Effects of Mn addition on the two-body abrasive wear behavior of Fe-3.0wt% B alloy, *Wear* 303 (2016) 243–251.
- [43] A. Pal, Comments on “X-ray analysis of ZnO nanoparticles by Williamson Hall and size-strain plot methods, *Solid State Sci.* 13 (2011) 251–256 (107060).
- [44] G. Liu, G.J. Zhang, F. Jiang, et al., Nanostructured high-strength molybdenum alloys with unprecedented tensile ductility, *Nat. Mater.* 12 (2013) 344–350.
- [45] Q. Chu, M. Zhang, J. Li, et al., Experimental investigation of explosion-welded CP-Ti/Q345 bimetallic sheet filled with Cu/V based flux-cored wire, *Mater. Des.* 67 (2015) 606–614.
- [46] Z. Gu, X. Su, W. Peng, et al., An important improvement of strength and ductility on a new type of CoCr2.5FeNi2TiW0.5 high entropy alloys under two different protective gases by selective laser melting, *J. Alloy. Compd.* 868 (1) (2021) 159088.
- [47] X. Yang, Y. Zhou, S. Xi, et al., Grain-anisotropied high-strength Ni\_6Cr\_4WFe\_9Ti high entropy alloys with outstanding tensile ductility, *Mater. Sci. Eng. A* 767 (Nov) (2019).
- [48] X. Yang, Y. Zhou, S. Xi, et al., Grain-anisotropied high-strength Ni\_6Cr\_4WFe\_9Ti high entropy alloys with outstanding tensile ductility, *Mater. Sci. Eng. A. Struct. Mater. Properties, Misrostruct. Process.* (2019) (767).
- [49] J. Chuang, Crack growth behaviour of heat-treated 4140 steel in air and gaseous hydrogen, *Int. J. Fatigue* 20 (7) (1998) 531–536.